RSC Advances

PAPER

View Article Online
View Journal | View Issue

Check for updates

Cite this: *RSC Adv.*, 2025, **15**, 231

Design, synthesis, anticancer activity and molecular docking of quinoline-based dihydrazone derivatives†

Jia-Xing Lu,[a] Hai-Rong Lan,[a] Dai Zeng,[a] Jun-Ying Song,[b] Ya-Ting Hao,[a] Ai-Ping Xing,*[a] Ao Shen*[a] and Juan Yuan *[a]

Based on the biologically active heterocycle quinoline, we successfully synthesized a series of quinoline-based dihydrazone derivatives (**3a–3d**). ^{1}H NMR, ^{13}C NMR, ESI-HRMS, IR, element analysis, UV/Vis spectroscopy and fluorescence spectroscopy were performed to comprehensively characterize their chemical structures, spectral properties and stability. Nitrosamine impurities were not detected in **3a–3d**, and the systemic toxicological assessment indicated that the toxicity of **3a–3d** was lower. Furthermore, their anticancer activity was evaluated by MTT, AO/EB double staining, apoptosis detection and ROS detection. The time-dependent UV/Vis spectra revealed that **3a–3d** had good stability in solution. For all the newly synthesized compounds, cytotoxic activities were carried out against human gastric cancer cell line BGC-823, human hepatoma cell line BEL-7402, human breast cancer cell line MCF-7 and human lung adenocarcinoma cell line A549 as well as human normal liver cell line HL-7702. MTT assay indicated that all the tested compounds exhibited important antiproliferative activity against selected cancer cell lines with IC_{50} values ranging from 7.01 to 34.32 μM, while none of them had obvious cytotoxic activity to human normal liver cell line HL-7702. Further, the most potent compound **3c** displayed stronger antiproliferative activity against all the selected cancer cell lines than the clinically used anticancer agent 5-FU. Especially, **3b** and **3c** displayed cytotoxic activity against MCF-7 cells with IC_{50} values of 7.016 μM and 7.05 μM, respectively. AO/EB double staining, flow cytometry and ROS detection suggested that **3b** and **3c** could induce MCF-7 cell apoptosis in a dose-dependent manner. Molecular docking suggests that **3b** and **3c** could bind with DNA *via* partial insertion. Additionally, molecular docking also suggests that CDK2 may be one of the targets for **3b** and **3c**. In a word, **3b** and **3c** could be suitable candidates for further investigation as chemotherapeutic agents in cancer treatment.

Received 27th September 2024
Accepted 17th December 2024

DOI: 10.1039/d4ra06954d

rsc.li/rsc-advances

Open Access Article. Published on 02 January 2025. Downloaded on 3/17/2026 5:53:47 PM.
This article is licensed under a Creative Commons Attribution-NonCommercial 3.0 Unported Licence.

1. Introduction

Cancer is a complicated disease, the rising incidence of which is seriously affecting our health.[1] Chemotherapy, as one of the most important treatment pathways for cancer,[2] has always been of great concern for researchers and clinical doctors. The development of anticancer agents with better treatment efficiency and fewer clinical side effects has attracted more and more attention of medicinal chemists.[3] N-heterocycles play a significant role in the design and synthesis of chemotherapy drugs. Quinoline and its derivatives, as a significant class of pharmaceutically active heterocyclic compounds, demonstrated diverse pharmaceutical activities, such as antiviral,[4] anticancer,[5,6] inhibitor,[7] antihypertensive,[8] antibacterial,[9,10] antimalarial[11] and others. Moreover, quinoline rings are found in various natural products, especially in alkaloids.[12,13] So, quinoline derivatives have attracted enormous attention of chemists and biologists. Meanwhile, hydrazones have attracted continuous attention in the medical field because of their good biological activity and reactivity.[14–18] The hydrazone moiety cannot only improve the flexibility of a chemical structure to avoid steric hindrance,[19] but also be the linker to merge functional groups together. Therefore, hydrazone moieties are often used as an active building block in antiviral and anticancer agents.[20,21] Quinoline-based hydrazone derivatives are highly important because of the structural flexibility and pharmacological activities. To our knowledge, a large number of quinoline-based hydrazone derivatives have been studied for their potential anticancer activity (Fig. 1).[20,22–26] However, we found that anticancer compounds that integrate two quinoline units into one molecule *via* hydrazone bonds have not been reported so far. Generally speaking, the number of active functional groups in a compound will be beneficial for its biological

[a]*School of Pharmacy, Henan University of Chinese Medicine, Zhengzhou 450046, China. E-mail: hn_xap@163.com; 18515912322@163.com; hnzz_yuan@hactcm.edu.cn*

[b]*Academy of Chinese Medical Sciences, Henan University of Chinese Medicine, Zhengzhou 450046, China*

† Electronic supplementary information (ESI) available. See DOI: https://doi.org/10.1039/d4ra06954d

© 2025 The Author(s). Published by the Royal Society of Chemistry

Open Access Article. Published on 02 January 2025. Downloaded on 3/17/2026 5:53:47 PM.
This article is licensed under a Creative Commons Attribution-NonCommercial 3.0 Unported Licence.

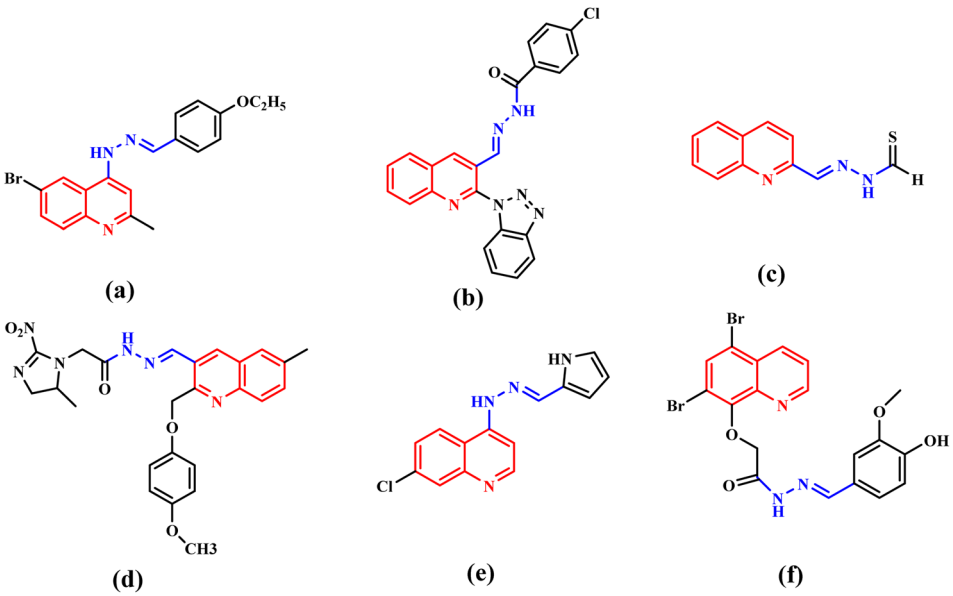

Fig. 1 Anticancer agents (a–f) containing quinoline hydrazone moieties.

activity. Dihydrazone structure makes it possible to increase the number of active functional groups in a molecule, which is expected to improve its biological activity. Based on these facts, supported by our ongoing research for new anticancer agents,[27] a series of new quinoline-based dihydrazone derivatives (**3a–3d**) linked by pyrimidine skeleton were designed, synthesized and investigated for their anticancer properties. Since nitrosamine impurities were detected in pharmaceuticals in 2018,[28] people have become aware of these impurities in raw materials. Since **3a–3d** are dihydrazone derivatives, nitrosamine impurities were evaluated and detected. Systemic toxicological evaluation of antitumor drug activity is very important because most chemotherapeutic cancer agents are non-specific in action; besides attacking tumors, they rapidly demolish normally dividing cells, and can cause extensive collateral side effects.

Quinoline derivatives have been revealed to exert anticancer effects through various mechanisms, which involved disruption of cell migration, growth inhibitors by cell cycle arrest, inhibition of angiogenesis, apoptosis and modulation of nuclear receptor responsiveness.[29–33] In addition, it has been reported that many quinoline derivatives exhibit significant anticancer activity through DNA binding.[20,34] Deviations within the CDK pathway have been observed in various types of cancer.[35,36] CDKs form complexes with cyclins to efficiently regulate tumour growth. CDKs have recently emerged as an extremely promising drug target for treating malignant tumours due to their involvement in various processes such as RNA processing, proliferation, and cell survival.[37–39] Therefore, developing anticancer drugs with CDK inhibitory activity is increasingly attracting attention. CDK inhibitors have advanced to the third generation, including palbociclib, ribociclib, and abemaciclib. Because they can selectively inhibit CDK4/6, they are also known as CDK4/6 inhibitors. Many non-selective CDK inhibitors, such as milciclib, dinaciclib and NU6300 (Fig. 2), which contain amino-substituted heterocyclic scaffold, have played a crucial role in developing binding affinity on CDK2.[40] **3a–3d** also contain amino-substituted heterocyclic scaffolds, the molecule docking study was performed to explain whether **3a–3d** also interact with CDK2. These docking results may indicate that **3a–3d** has potential anticancer activity by inhibiting the activity of CDKs. Herein, on the basis of preliminary screening of the cytotoxic activity of **3a–3d** by MTT assay, **3b** and **3c** were further investigated for their pro-apoptotic effect, DNA-binding and CDKs inhibitory activities.

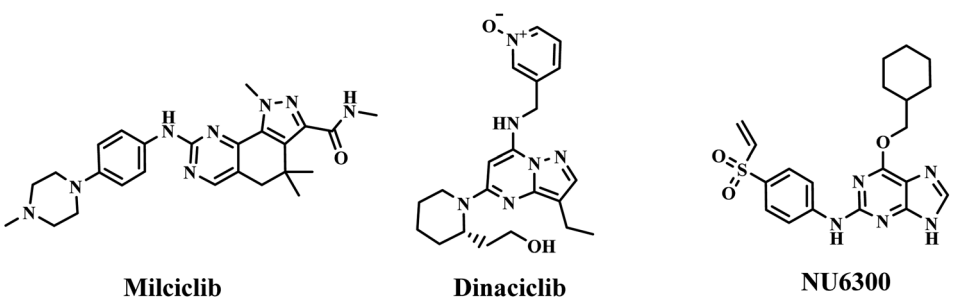

Fig. 2 CDK inhibitors containing amino-substituted heterocyclic scaffold.

© 2025 The Author(s). Published by the Royal Society of Chemistry

Open Access Article. Published on 02 January 2025. Downloaded on 3/17/2026 5:53:47 PM. This article is licensed under a Creative Commons Attribution-NonCommercial 3.0 Unported Licence.

2. Experimental section

2.1. Materials and measurements

20 Female Blab/c mice (age 6 weeks) of SPF grade were obtained from Changsheng Biotechnology Co., Ltd (SCXK 2020-0001). The animals were housed and kept under a temperature-controlled room (22–25 °C), with 12 : 12 h light–dark cycle and free access to food and water. The experimental protocol was submitted and approved by the Animal Management and Welfare Ethics Committee of Henan University of Chinese Medicine. All chemical raw materials used were obtained from Beijing Inno Chem Science &Technology Co., Ltd (Beijing, China). Biochemical reagents were purchased from Solarbio Science & Technology Co., Ltd. All the above reagents were used directly as purchased. All cell lines (HL-7702, MCF-7, BGC-823, BEL-7402 and A549) were purchased from the Obio Technology (Shanghai) Corp., Ltd (Shanghai, China). Tris-HCl-NaCl buffer solution (0.05 M Tris-HCl/0.1 M NaCl, pH 7.4) was prepared by using ultrapure water. UV/Vis spectra were performed within the range of 200–750 nm on a Shimadzu UV-3600i plus spectrophotometer (Japan). The FLS1000 spectrometer (UK) was used to record fluorescence spectra. ^{1}H NMR and ^{13}C NMR were performed on a Bruker AVANCE III spectrometer (Germany, 500 MHz). ESI-HRMS was carried out on a Bruker Thermo Scientific Q Exactive high resolution mass spectrometry (Germany). Elemental analyses were determined on an Elementar Vario EL elemental analyzer. IR absorption spectra were measured in the range of 4000–400 cm^{-1} on a WQF-510A FTIR spectrophotometer. MTT assay was collected at 570 nm using a Thermo fisher Multiskan GO (America). AO/EB staining was performed under a Leica DMIL LED inverted fluorescence microscope (Germany). Cell apoptosis and ROS intensity were detected by a flow cytometry (Beckman coulter CytoFLEX, America).

2.2. Chemistry

The intermediates 4,6-dihydrazinylpyrimidine (**2a**) and 4,6-dihydrazinyl-2-phenylpyrimidine (**2b**) were similarly prepared by the reaction of 4,6-dichloropyrimidine (**1a**) or 4,6-dichloro-2-phenylpyrimidine (**1b**) with an excess of hydrazine hydrate.

The detailed synthesis process of **2a** was as follows: **1a** (10 mmol, 1.49 g) was dispersed in 10 mL hydrazine hydrate. Then, the mixture was slowly heated to 60 °C under stirring. White solid gradually precipitated during the stirring process. The reaction process was monitored by thin-layer chromatography (TLC). After the reaction was completed, the reaction solution was cooled overnight to promote complete precipitation. Finally, the product was filtered, washed with water and then dried, which was named 4,6-dihydrazinyl pyrimidine (**2a**), yield *ca.* 72.0%. The intermediate **2b** was also obtained by the same method, yield *ca.* 55.5%.

2.2.1 Synthesis of 3a–3d. The synthetic procedures of **3a–3d** were similar and displayed in Scheme 1, only the synthesis of **3a** was described in detail.

4,6-Bis(2-((*E*)-quinolin-2-ylmethylene)hydrazinyl)pyrimidine (**3a**).Quinoline-2-formaldehyde (2.1 mmol, 330 mg) and **2a** (1 mmol, 140 mg) were added to 20 mL ethanol solvent at room temperature. Then, the reaction mixture was heated and refluxed for 6 h, and yellow precipitation gradually appeared. Finally, the precipitation was filtered, washed thoroughly with ethanol and then purified by column chromatography (petroleum ether : ethyl acetate = 1 : 1) to give yellow solid, named compound **3a**, with a yield of *ca.* 54.0%. ^{1}H NMR (500 MHz, DMSO-d_6) δ 11.64 (s, 2H, NH), 8.47 (d, J = 8.7 Hz, 2H, $CH_{quinoline}$), 8.31 (s, 2H, CH=N), 8.28 (s, 1H, *N*–CH=N, $CH_{pyrimidine}$), 8.21 (d, J = 8.6 Hz, 2H, $CH_{quinoline}$), 8.02 (d, J = 1.5 Hz, 2H, $CH_{quinoline}$), 8.00 (d, J = 1.0 Hz, 2H, $CH_{quinoline}$), 7.77 (t, J = 7.0 Hz, 2H, $CH_{quinoline}$), 7.61 (t, J = 7.0 Hz, 2H, $CH_{quinoline}$), 7.08 (s, 1H, $CH_{pyrimidine}$). ^{13}C NMR (101 MHz, DMSO-d_6) δ 161.97, 158.48, 154.63, 148.01, 142.80, 137.20, 130.49, 129.25, 128.45, 128.11, 127.42, 117.78, 82.62. ESI-HRMS: m/z calculated for $[C_{24}H_{18}N_8+H]^+$: 419.17327, found: 419.17096. Elemental analysis (%): calcd for $C_{24}H_{18}N_8$ (**3a**): C 68.9, H 4.3, N 26.8; found: C 68.1, H 4.2, N 27.1. The melting point of **3a** is about 315 °C. IR (cm^{-1}, KBr): 3173, 3046, 2964, 2855, 1707, 1667, 1608, 1583, 1558, 1502, 1454, 1415, 1375, 1324, 1247, 1197, 1143, 1112, 985, 827, 746.

4,6-Bis(2-((*E*)-quinolin-8-ylmethylene)hydrazinyl)pyrimidine (**3b**). Yellow solid, yield: *ca.* 58.6%. ^{1}H NMR (500 MHz, DMSO-d_6) δ 11.35 (s, 2H, NH), 9.38 (s, 2H, CH=N), 8.96 (dd, J = 4.1, 1.7 Hz, 2H, $CH_{quinoline}$), 8.44–8.41 (dd, J = 4.0, 1.7 Hz, 2H, $CH_{quinoline}$), 8.41 (dd, J = 3.9, 1.5 Hz, 2H, $CH_{quinoline}$), 8.03 (dd, J = 8.1, 1.2 Hz, 2H, $CH_{quinoline}$), 7.75 (t, J = 7.7 Hz, 2H, $CH_{quinoline}$), 7.60 (dd, J = 8.3, 4.1 Hz, 2H, $CH_{quinoline}$), 7.01 (s, 1H, N–C=N, $CH_{pyrimidine}$), 5.72 (s, 1H, $CH_{pyrimidine}$). ^{13}C NMR (101 MHz, DMSO-d_6) δ 162.31, 158.11, 150.56, 145.72, 139.41, 137.07, 132.31, 129.49, 128.60, 127.20, 125.35, 122.31, 81.88. ESI-HRMS: m/z calculated for $[C_{24}H_{18}N_8+H]^+$: 419.17327, found: 419.17102. Elemental analysis (%): calcd for $C_{24}H_{18}N_8$ (**3b**): C 68.9, H 4.3, N 26.8; found: C 69.1, H 4.3, N 26.9. The melting point of **3b** is about 325 °C. IR (cm^{-1}, KBr): 3199, 2960, 2923, 2855, 1587, 1558, 1496, 1461, 1417, 1256, 1203, 1126, 1085, 1035, 989, 792, 652, 547.

2,2′-((1*E*,1′*E*)-((2-phenylpyrimidine-4,6-diyl)bis(hydrazin-2-yl-1-ylidene))bis(methanylylidene))diquinoline (**3c**). Yellow solid, yield: *ca.* 51.2%. ^{1}H NMR (500 MHz, DMSO-d_6) δ 11.79 (s, 2H, NH), 8.61 (d, J = 8.5 Hz, 2H, $CH_{quinoline}$), 8.43 (d, J = 5.2 Hz, 2H, $CH_{quinoline}$), 8.37 (s, 2H,CH=N), 8.14 (d, J = 8.6 Hz, 2H, $CH_{quinoline}$), 7.97 (d, J = 8.6 Hz, 2H, $CH_{quinoline}$), 7.86 (d, J = 8.6 Hz, 2H, $CH_{quinoline}$), 7.76 (d, J = 7.5 Hz, 2H, $CH_{quinoline}$), 7.60 (d, J = 6.9 Hz, 2H, $CH_{benzene}$), 7.54 (d, J = 7.2 Hz, 3H, $CH_{benzene}$), 7.14 (s, 1H, $CH_{pyrimidine}$). ^{13}C NMR (101 MHz, DMSO-d_6) δ 163.98, 163.16, 155.24, 148.40, 143.42, 138.64, 137.64, 131.78, 131.40, 131.07, 129.81, 129.38, 129.03, 128.70, 128.67, 127.99, 118.38, 81.72. ESI-HRMS: m/z calculated for $[C_{30}H_{22}N_8+H]^+$: 495.20457, found: 495.20236. Elemental analysis (%): calcd for $C_{30}H_{22}N_8$ (**3c**): C 72.8, H 4.5, N 22.7; found: C 71.5, H 4.3, N 22.9. The melting point of **3c** is about 327 °C. IR (cm^{-1}, KBr): 3203, 3039, 1663, 1604, 1592, 1563, 1533, 1504, 1461, 1411, 1388, 1182, 1147, 1112, 825, 748, 696.

8,8′-((1*E*,1′*E*)-((2-Phenylpyrimidine-4,6-diyl)bis(hydrazin-2-yl-1-ylidene))bis(methanylylidene))diquinoline (**3d**). Yellow solid, yield: *ca.* 67%. ^{1}H NMR (500 MHz, DMSO-d_6) δ 11.47 (s, 2H, NH), 9.43 (s, 2H, CH=N), 9.00 (d, J = 8.3 Hz, 2H, $CH_{quinoline}$), 8.44 (d,

Open Access Article. Published on 02 January 2025. Downloaded on 3/17/2026 5:53:47 PM.
This article is licensed under a Creative Commons Attribution-NonCommercial 3.0 Unported Licence.

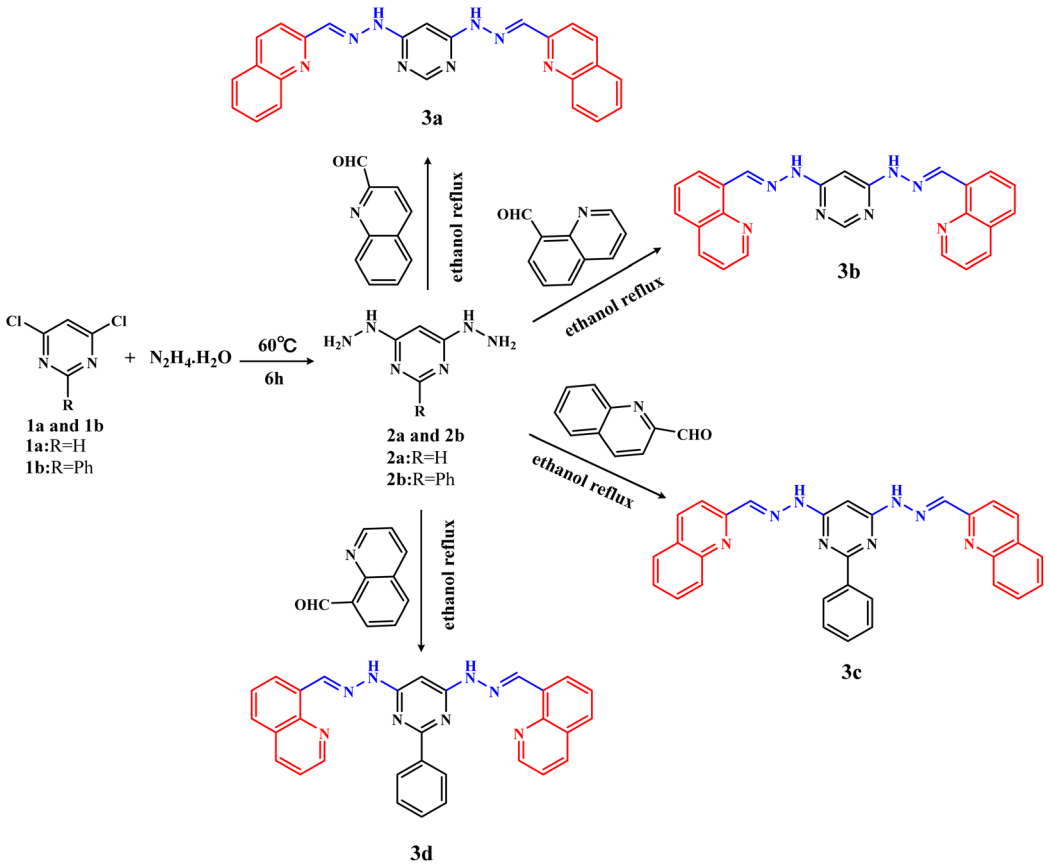

Scheme 1 Synthesis of **3a–3d**.

J = 7.5 Hz, 2H, $CH_{quinoline}$), 8.42 (d, J = 7.3 Hz, 2H, $CH_{quinoline}$), 8.34 (d, J = 7.2 Hz, 2H, $CH_{quinoline}$), 8.02 (d, J = 6.4 Hz, 2H, $CH_{quinoline}$), 7.77 (d, J = 7.0 Hz, 2H, $CH_{quinoline}$), 7.63–7.57 (d, J = 6.9 Hz, 2H, $CH_{benzene}$), 7.49 (d, J = 6.4 Hz, 3H, $CH_{benzene}$), 7.03 (s, 1H, $CH_{pyrimidine}$). ^{13}C NMR (101 MHz, DMSO-d_6) δ 163.09, 162.88, 158.97, 151.37, 150.68, 145.54, 139.16, 137.24, 132.50, 130.87, 129.45, 128.70, 128.13, 127.60, 127.03, 125.35, 122.57, 81.15. ESI-HRMS: m/z calculated for $[C_{30}H_{22}N_8+H]^+$: 495.20457, found: 495.20380. Elemental analysis (%): calcd for $C_{30}H_{22}N_8$ (**3d**): C 72.8, H 4.5, N 22.7; found: C 72.6, H 4.7, N 23.1. The melting point of **3d** is about 271 °C. IR (cm^{-1}, KBr): 3178, 3030, 2998, 1723, 1597, 1589, 1573, 1560, 1496, 1407, 1199, 1126, 825, 788, 755, 694, 567.

2.3. Detection of nitrosamine impurities

The calibration curves for NDMA and NDEA were prepared at concentrations of 0.1, 0.3, 1, 2, 5, 10, 20, 50, 100, 300 and 1000 ng mL^{-1}. The **3a**, **3b**, **3c** and **3d** were dissolved in DMSO at a concentration of 5 mg mL^{-1} at 37 °C and incubated. In each EP tube, 100 μL of the 5 mg mL^{-1} above compounds was added, followed by 150 μL of DMSO and 250 μL of acetonitrile. The mixture was vortexed and the resulting sample solution was obtained for using. Chromatographic conditions: run time: 6 min; column temperature: 40 °C; injection volume: 5 μL. Chromatographic column: C18, 2.7 μm, 3.0 × 75 mm. Mass spectrometric conditions: ion source: APCI; scan time: 6 min; ion source temperature: 350 °C; CUR: 30 psi; gas 1 : 60 psi; CAD: MediμM; detection mode: MRM (multiple reaction monitoring); EP: 10.0 V; CXP: 10.0 V.

2.4. Systemic toxicological evaluation

2.4.1. Determination of the effect of 3a–3d on body and organ weight. Body weights (n = 4 mice/group) were determined at the beginning and end of treatment. Control (n = 4 mice/group), **3a** (n = 4 mice/group), **3b** (n = 4 mice/group), **3c** (n = 4 mice/group), **3d** (n = 4 mice/group). All systemic toxicological analyses were also performed with 5 healthy animal groups (n = 4 mice/group) treated **3a** 1000 mg per kg per day (i.g.), **3b** 1000 mg per kg per day (i.g.), **3c** 1000 mg per kg per day (i.g.), **3d** 1000 mg per kg per day (i.g.) for a string of 14 days; the mice were anesthetized (1.5% isoflurane) for blood collection and then dissected to extract and weigh the liver, spleen, and kidneys of each group.

2.4.2. Determination of the effect of 3a–3d on biochemical parameters. To investigate whether the drug has an impact on the liver and kidney organs of mice, we selected two indicators, aspartate aminotransferase (AST) and alanine aminotransferase (ALT), to evaluate the impact on the liver, and urea chosen and creatinine, which are important indicators of kidney function, for detection. In this experiment, blood collection is performed *via* the orbital venous sinuses. The collected blood was left at

© 2025 The Author(s). Published by the Royal Society of Chemistry

Open Access Article. Published on 02 January 2025. Downloaded on 3/17/2026 5:53:47 PM. This article is licensed under a Creative Commons Attribution-NonCommercial 3.0 Unported Licence.

room temperature for 40 min, then centrifuged at 3000 rpm for 10 min to collect the serum for detection.

2.4.3. Histopathological analysis. Weighed the livers, spleens, and kidneys from different groups, fixed them with 10% formaldehyde, then dehydrated them with alcohol, embedded them in paraffin, cut them into sections, stained them with hematoxylin and eosin, and finally observed them under an optical microscope to observe if there were any pathological changes.

2.5. Biological evaluation

2.5.1. Stability study. The stock solution of **3a–3d** in DMSO was added into Tris-HCl-NaCl buffer (5.0 mL, 0.05 M Tris-HCl/0.1 M NaCl, pH 7.4) to prepare a working solution with a final concentration of 0.1 μM. The amount of DMSO in the working solution is no more than 1%. The time-dependent UV/Vis absorption spectra of **3a–3d** (0 h, 24 h and 48 h) were recorded using a 1.0 cm quartz cuvette on a Shimadzu UV-3600i plus spectrophotometer. Meanwhile, the stability of **3a–3d** (0 h, 24 h and 48 h) in DMSO was also investigated using the same method. The stability of **3a–3d** was determined by observing the changes of peak position and peak intensity in absorption spectra.

2.5.2. Cytotoxic MTT assay. The antiproliferative activity of **3a–3d** was evaluated by MTT assay. BGC-823, BEL-7402, MCF-7, A549 and HL-7702 cell lines were selected for the experiments. 5-FU was used as the positive control. DMEM with 10% fetal bovine serum was used as culture medium. First, cells with appropriate density were precultured into 96-well plates for 24 h at 37 °C, 5% CO_2. Second, **3a–3d** were added to the above 96-well plates at concentration gradients (1.25, 2.5, 5, 10 and 20 μg mL^{-1}). After cells were incubated continuously for 48 h, MTT solution (20 μL, 5 mg mL^{-1}) was added into each well for another 4 h. Finally, DMSO (150 μL) was added into each well, and the absorbance of the converted dye in living cells was measured at a wavelength of 570 nm (ref. 41) using a microplate reader. The inhibition rate was calculated according to eqn (2). The IC_{50} values were calculated according to the inhibition rate at a different concentration. Three independent experiments were performed and IC_{50} values were showed as mean ± SD.

$$\text{Inhibition rate (\%)} = 1-(OD_{sample} - OD_{blank})/(OD_{negative} - OD_{blank}) \times 100\% \quad (1)$$

2.6. Apoptosis detection

2.6.1. AO/EB double staining. MCF-7 cells were inoculated in 6-well plates and incubated at 37 °C for 24 h. Then **3b** or **3c** with varying concentrations (3.5 μM, 7 μM and 10.5 μM) was added to the cell culture plate and incubated for another 24 h. After incubation, MCF-7 cells were washed with PBS for 2–3 times and stained with AO/EB dye (100 μL, 0.1 mg mL^{-1}) for 3–5 min under dark conditions. After a final wash with PBS for 2–3 times, the cells were observed immediately under an inverted fluorescence microscope.

2.6.2. Flow cytometric analysis. Annexin V-FITC/PI Apoptosis Detection Kit was used to evaluate the induced apoptosis. MCF-7 cells were incubated for 48 h with varying concentrations **3b** or **3c** (3.5 μM, 7 μM and 10.5 μM), respectively. Then they were trypsinized and no fewer than 10^6 cells were collected. Then, the collected cells were incubated 5 min in a mixed solution of annexin V-FITC (5 μL) and propidium iodide (PI, 10 μL) at room temperature in the dark. The intracellular fluorescence intensity was analyzed immediately by flow cytometry at a 488 nm single beam laser. FlowJo software was used to process the data.

2.6.3. Intracellular measurements of reactive oxygen species (ROS). The intracellular reactive oxygen species generated within MCF-7 cells upon treatment with **3b** or **3c** were evaluated using fluorescent dye 2,7-dichlorodihydrofluorescein diacetate (DCFH-DA, ROS Assay Kit, Solarbio, Beijing, China) on a flow cytometer. In the experiment, 6-well plates were used to culture MCF-7 cells to investigate the effect of **3b** or **3c** on the production of reactive oxygen species in cells. The specific experimental process is as follows: MCF-7 cells were treated with **3b** or **3c** (3.5 μM and 7 μM) and incubated for 24 h at 37 °C, 5% CO_2. After incubation, cells were collected, washed and further incubated with DCFH-DA (5 μM) in serum-free DMEM for another 30 min at 37 °C. After that, these cells were washed again with PBS and tested on a flow cytometer.

2.7. Molecular docking

Compounds were subjected to molecular docking using AutoDock Tools-1.5.6 software. Firstly, the crystal structures of receptors, DNA (PDB ID: 2MG8), CDK1 (PDB ID:6GU7), CDK2 (PDB ID: 4BGH), CDK4 (2W9Z), CDK8 (5i5Z), were downloaded from Protein Data Bank (**http://www.rcsb.org./pdb**). The molecular structures of ligands were drawn by ChemDraw and converted into MOL2 format by Chem3D. Secondly, the structures of receptors and ligands were all optimized by AutoDock Tools-1.5.6 software and saved as PDBQT format. Then, the appropriate boxes for the interactions of ligand and receptor were set and the set parameters were saved as conf files. Molecular docking was performed, analyzed, and the optimal conformation was selected. The binding modes of tested compounds with DNA or CDKs were conducted to explain the biological results and further understand the binding direction and interaction. The pose with good hydrogen bond geometry and low energy conformation was screened for further analysis. Docking structures and figures were analyzed and generated using the PyMOL molecular graphic system and Discovery Studio 4.5.

3. Results and discussion

3.1. Synthesis and spectroscopic characterization

The target compounds **3a–3d** were synthesized by a two-step reaction (Scheme 1). In brief, the intermediates **2a** and **2b** were synthesized by nucleophilic substitution reaction, then **3a–3d** were synthesized by condensation reaction of **2a** or **2b** with quinoline aldehydes, respectively. During the synthesis process, the reaction process was monitored by thin layer chromatography. **3a–3d** were all purified by column

Open Access Article. Published on 02 January 2025. Downloaded on 3/17/2026 5:53:47 PM. This article is licensed under a Creative Commons Attribution-NonCommercial 3.0 Unported Licence.

Table 1 ^{1}H NMR, ^{13}C NMR and FTIR signals for **3a–3d** and their assignments

	Amide –NH–		Imine –CH=N–		
Compound	^{1}H NMR δ	FTIR cm^{-1}	^{1}H NMR δ	^{13}C NMR δ	FTIR cm^{-1}
3a	11.64	3173	8.31	142.80	1608
3b	11.35	3199	9.38	13 941	1597
3c	11.79	3203	8.37	138.64	1604
3d	11.47	3178	9.43	139.16	1589

chromatography using the same eluent, with yields above 50%. It was found that hydrazine hydrate is not only the reactant, but also the solvent of the intermediates (**2a**, **2b**) reaction. If ethanol is used as the reaction solvent, the intermediates **2a** and **2b** cannot be obtained successfully, only the monosubstituted pyrimidine hydrazine can be obtained.

^{1}H NMR, ^{13}C NMR, ESI-HRMS, IR (Fig. S1–S16†), melting, UV/Vis spectra (Fig. S17†) and fluorescence spectra (Fig. S18†) were performed to characterize the chemical structures and spectral properties of **3a–3d**. The important spectral data of –NH– and –CH=N– and their assignments were listed in Table 1. Characteristic signals for the quinoline ring are multiple peaks at 9.00–7.60 ppm in ^{1}H NMR spectra. The presence of the hydrazone group was confirmed by broad signal of NH protons and CH=N protons at 11.79–11.35 ppm, 9.43–8.31 ppm respectively. For **3c** and **3d**, the presence of the benzene ring was supported by the chemical shift at 7.63–7.49 ppm in ^{1}H NMR spectra. Compounds **3a–3d** are symmetric and the results of ^{1}H NMR were consistent with their structures. In the ESI-HRMS analysis, the observed molecular ion peaks of **3a–3d** were $[M + H]^{+}$. The IR absorption bands of the typical functional groups in **3a–3d** are very similar. The IR spectra of **3a–3d** showed similar absorption bands. The N–H stretching vibrations are in the range of 3173–3203 cm^{-1}, and the C=N stretching vibrations were observed in the region of 1589–1608 cm^{-1}. Conventional UV/Vis spectra of **3a–3d** were shown in Fig. S17.† The UV/Vis spectra are similar and the structural difference of **3a–3d** has little effect on positions of absorption peaks. Because of the presence of C=N functional groups and big conjugated system, **3a–3d** all demonstrate strong absorption peaks near 205 nm, which are assigned to the transition of lone pair electrons from unbonded heteroatoms to π^* antibonding orbitals. Meanwhile, the conjugate system is usually attributed to $\pi \rightarrow \pi^*$ transition. As a result, the absorption peaks near 205 nm of **3a–3d** are generated by $n/\pi \rightarrow \pi^*$ transition. The fluorescence spectra of **3a–3d** were recorded in Fig. S18† (EX: 360 nm). As shown in Fig. S18,† the fluorescence spectra of **3a–3d** were similar too. The fluorescence emission peaks near 390 nm are attributed to the existence of C=N functional groups. The emission peaks near 450 nm are due to quinoline chromophore.

3.2. Risk assessment and detection of nitrosamine contaminants

3.2.1. Risk assessment of nitrosamine impurities. Multiple compounds featuring secondary amine structures were

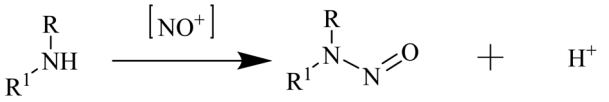

Scheme 2 Generalised nitrosation of secondary amines under acidic conditions.

discovered: **2a**, **2b**, **3a**, **3b**, **3c** and **3d**. Despite the involvement of amines in the synthesis procedure, the formation of *N*-nitrosamine impurities mentioned in Scheme 2 requires nitrosamines or other nitrosating agents. However, no nitrosamines or nitrosating agents were used in the synthesis route. Hence, the risk of introducing *N*-nitrosamine impurities of **3a–3d** is extremely low. And following the toxicological evaluation of nitrosamines, even if the amine precursors are transformed into corresponding nitrosamine impurities under suitable circumstances, they are not regarded as traditional concern cohort nitrosamine impurities, as follows: the *in vivo* carcinogenic route of nitrosamines, for instance, NDMA (Scheme S1†), typically requires an α-proton to be oxidized (hydroxylated) to trigger demethylation (other diarylamino *N*-nitrosamines are dealkylated) and then form an active methylnitronium ion and a methyl cation. The methyl nitronium ion and the methyl cation are powerful methylating agents that can methylate DNA. No α-protons were identified in any of the possible nitrosamine molecules generated during the synthesis steps, and they are not considered to form stable alkyl or aromatic nitronium ions or cations. Therefore, the acceptable intake level (AI value) is suggested to be 1500 ng per day according to the CPCA method. Meanwhile, considering hydrazine as a raw material for the synthesis process, the presence of ethyl donor ethyl acetate and ethanol may react with hydrazine to form NDEA's amine precursor diethylamine. At the same time, hydrazine reacts with substances containing methyl groups (dichloromethane/anhydrous methanol) to form NDMA's amine precursor dimethylamine. Although no nitrosating agents or nitrates are used in the synthesis process, the carcinogenic risks of NDEA and NDMA are extremely high. Therefore, verification tests for NDEA and NDMA are necessary. All in all. All impurities that could arise are aggregated into in Table S1.†

3.2.2. Detection of NDMA and NDEA in 3a–3d. To enhance credibility, samples that had been stored in the laboratory for 1 year were chosen for detection. Compared with the standard peaks of NDMA and NDEA in Fig. S19a and b,† no NDMA and NDEA were detected in **3a–3d** (Fig. S19c–j†).

3.3. Systemic toxicological evaluation

3.3.1. Effects of 3a–3d on mice body weight and organ weight. The toxicological evaluation of anti-tumor drugs is critical because the effects of most chemotherapies are non-specific; in addition to attacking tumor cells, they can quickly destroy normal dividing cells and may cause widespread side effects.[42] Monitoring the weight of each group of mice for 14 days, we found that the weight of the treated group was not significantly different from that of the control group. Similarly,

 © 2025 The Author(s). Published by the Royal Society of Chemistry

Open Access Article. Published on 02 January 2025. Downloaded on 3/17/2026 5:53:47 PM. This article is licensed under a Creative Commons Attribution-NonCommercial 3.0 Unported Licence.

Table 2 The effects of **3b** and **3c** on mice body weight and organ weight

Treatment	Initial weight (g)	Final weight (g)	Liver (mg)	Spleen (mg)	Kidney (mg)
Control	18.22 ± 0.53	23.10 ± 0.20	500 ± 30.1	88 ± 3.3	200 ± 11.1
3a	18.66 ± 0.25	23.65 ± 0.33	521 ± 19.7	78 ± 2.7	212 ± 7.7
3b	18.31 ± 0.34	22.18 ± 0.45	517 ± 11.7	80 ± 3.6	207 ± 6.6
3c	18.56 ± 0.33	22.35 ± 0.27	523 ± 16.1	83 ± 4.5	218 ± 9.9
3d	19.00 ± 0.78	24.66 ± 0.95	540 ± 15.5	89 ± 3.3	225 ± 6.3

the weight of mice's liver, spleen, and kidneys in each group was not significantly different from that of the control group. The changes in mice weight and organ weight are summarized in Table 2. Weight changes are an essential indicator for evaluating a drug's toxicity. The weight and organ quality of mice in the treated group were not significantly lower than those in the control group, and this experimental result indicates that the toxicity of **3a–3d** is relatively tiny.

3.3.2. Effects of 3a–3d on biochemical indicators. The liver and kidneys are the most critical detoxification and excretion organs, and most anti-cancer drugs produce various toxic effects, such as nephrotoxicity and hepatotoxicity.[43] Based on this, we chose the liver and kidneys for biochemical experiments, where the evaluation indicators for the liver were ALT and AST, and the evaluation indicators for the kidneys were urea and creatinine. The results in Table 3 and Fig. 3 showed no significant differences in the biochemical parameters between the treatment and standard groups. This proved that the biochemical parameters of the liver and kidneys would not change at the given dosage (1000 mg kg^{-1}) in this experiment.

3.3.3. Histopathological analysis. The histopathological examination of liver, spleen, and kidney tissues in the control and treatment groups showed no significant morphological changes, consistent with the results of biochemical indicators (Fig. 4).

3.4. Biological evaluation

3.4.1. Analysis of stability. Stability is essential to evaluate biological activity of compounds. The absorption spectra of **3a–3d** in Tris-HCl-NaCl buffer solution at different times (0 h, 24 h and 48 h) were investigated and recorded in Fig. S20–S23.† To investigate the stability of **3a–3d** in different solvents, the absorption spectra of **3a–3d** in phosphate-buffered saline (PBS) at different times (0 h, 24 h and 48 h) were also investigated and recorded in Fig. S23–S26.† To investigate the long-term stability of the compounds under different conditions, we also examined the absorption spectra of various batches stored in a 4 °C refrigerator for 3 months, 6 months and 1 year in PBS and recorded the results in Fig. S28–S31.† The results showed that **3a–3d** had absorption peaks around 205 nm in both room temperature storage and 4 °C refrigerator storage conditions, and their absorption intensities did not show significant changes and could be responsible for their biological activity.

3.4.2. Cytotoxicity *in vitro*. The *in vitro* cytotoxicity of **3a–3d** was evaluated against selected cancer cell lines (human gastric cancer cell line BGC-823, human hepatoma cell line BEL-7402, human breast cancer cell line MCF-7 and human lung adenocarcinoma cell line A549) by MTT assay, with 5-FU as positive control. Moreover, normal human liver cell line HL-7702 was chosen to investigate the cytotoxic activity of **3a–3d** against normal human cell lines. The IC_{50} values were listed in Table 4

Table 3 The values of biochemical indicators in different groups

Treatment	ALT (U L^{-1})	AST (U L^{-1})	BUN (mg dL^{-1})	CREA (μM)
Control	57.23 ± 0.02	114.65 ± 0.15	15.08 ± 0.32	10.85 ± 0.12
3a	54.66 ± 0.15	115.38 ± 0.23	16.08 ± 0.21	10.44 ± 0.45
3b	53.21 ± 0.38	121.60 ± 1.15	19.74 ± 0.48	12.34 ± 0.78
3c	54.35 ± 0.35	116.45 ± 2.35	21.72 ± 0.36	13.42 ± 0.23
3d	56.38 ± 0.64	119.26 ± 1.24	15.96 ± 0.63	14.21 ± 0.97

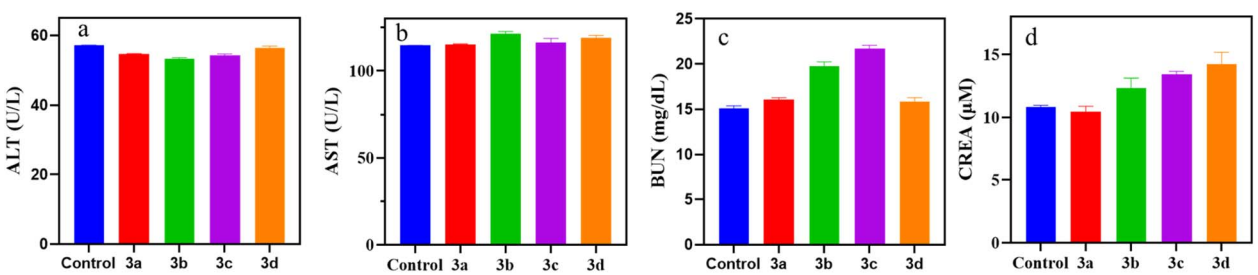

Fig. 3 Biochemical indicators of different groups (a: ALT; b: AST; c: BUN; d: CREA).

Open Access Article. Published on 02 January 2025. Downloaded on 3/17/2026 5:53:47 PM. This article is licensed under a Creative Commons Attribution-NonCommercial 3.0 Unported Licence.

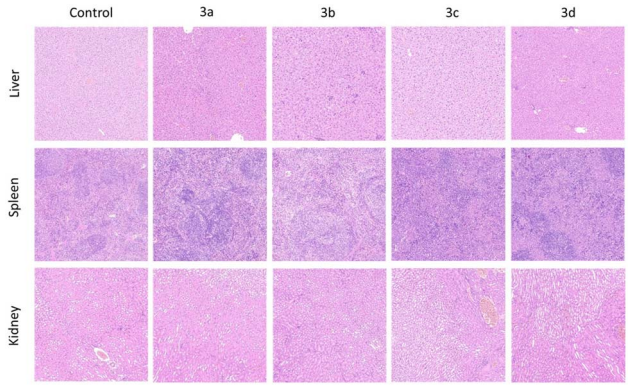

Fig. 4 H&E staining of different organ groups (liver, spleen, kidney).

and Fig. S32.† The results demonstrated that **3a–3d** exhibited important antiproliferative activity against selected cancer cell lines, with IC_{50} values in the range of 7.01–34.32 μM. Among them, **3a** exhibited weak cytotoxicity against MCF-7, BEL-7402 cell lines. **3b–3d** showed moderate cytotoxicity against MCF-7, BEL-7402, A549, BGC-823 cell lines, with IC50 values of 7.01 and 26.79 μM, respectively. It is mentioning that the above compounds showed no obvious cytotoxic activity to HL-7702, except **3b** which was slightly cytotoxic. The results revealed that **3a–3d** all had potential anticancer activity, while exhibiting no discernible effect on normal human liver cells HL-7702. **3b–3d** displayed stronger antiproliferative activity against MCF-7 cells than 5-FU and Erlotinib (IC_{50} = 7.01 ± 0.26 μM, 7.05 ± 0.05 μM and 10.39 ± 0.52 μM). Compared with benzo quinoline aromatic hydrazone derivative (compound 1, IC_{50} = 19.85 ± 4.15 μM)[44] and quinoline hydrazone derivative (compound 18b, IC_{50} = 14.1 μM),[20] **3b** and **3c** showed better antiproliferative activity against MCF-7 cells. Hence, as the potential anticancer compounds, **3b** and **3c** were selected for further anticancer mechanism exploration.

In addition, we noticed that **3c** showed stronger antiproliferative activity than **3a** against all the selected cancer cell lines. Similarly, **3d** also displayed better antiproliferative activity than **3b** against BGC-823, BEL-7402 and A549. The similar antiproliferative activities in these two different quinoline-based hydrazone derivatives indicated that the introduction of phenyl on pyrimidine skeleton could significantly enhance anticancer activity probably due to the increase of conjugated structure.

3.5. Apoptosis detection analysis

3.5.1. Apoptosis assay with AO/EB staining. AO/EB double staining is commonly used to evaluate the changes in apoptotic cell morphology.[45] Apoptotic and necrotic cells can be identified using fluorescence microscopy. The apoptotic cells usually show apoptotic features such as nuclear shrinkage and chromatin condensation. In the late stage of apoptosis, the nucleus can break into fragments, producing apoptotic bodies. Acridine Orange (3,6-bis(dimethylamine)acridine, AO) is a fluorescent dye, which can penetrate the intact cell membranes and embed DNA in the nucleus to produce yellow-green or orange fluorescence. So, AO is mainly used to label live cells or early apoptotic cells. While ethidium bromide (3,8-diamino-5-ethyl-6-phenylphenanthridinium bromide, EB) can only penetrate cells with damaged cell membranes, embed nucleus DNA to cause red fluoresce, which makes EB is mainly used to label dead cells or late apoptotic cells.[46] Fig. 5 depicted the morphological changes of AO/EB dual-stained MCF-7 cells treated with different concentrations of **3b** or **3c** (0 μM for control, 3.5 μM, 7 μM and 10.5 μM). Three independent experiments were performed on each compound, the results were similar. In the control group, the normal morphology and homogeneous green fluorescence were observed. However, when MCF-7 cells were exposed to **3b** (Fig. 5a) or **3c** (Fig. 5b), an increasing number of cells with apoptotic features were observed in a concentration-dependent manner. The analysis preliminarily demonstrated that both **3b** and **3c** could trigger MCF-7 cells apoptosis.

3.5.2. Apoptosis detection by flow cytometry. Annexin V-FITC/PI dual staining can be used to quantify the different cell phenotypes that occur during apoptosis.[47] Herein, annexin V-FITC/PI dual staining experiment was performed by flow cytometry (Fig. 6) to further assess the apoptosis of MCF-7 cells promoted by **3b** and **3c**. Three independent experiments were conducted with similar results. The average values of three experimental results were given below and analysed. The results displayed that the concentration-dependent increase in apoptotic cells when MCF-7 cells were incubated with **3b** or **3c** gradient concentrations (3.5 μM, 7 μM and 10.5 μM) for 48 h. For **3b**, the average percentage of MCF-7 cells in the Q3 zone was remarkably increased by 31.4%, 38.5% and 55.9%, respectively. While, for **3c**, the average percentage of MCF-7 in the Q3 zone was gradually increased by 22.2%, 23.0% and 25.2%, respectively. Moreover, with the increase of concentration, the total apoptosis average percentage both in the Q2 and the Q3 zones for **3b** and **3c** were also increased by 34.2%, 46.5%, 60.0% and

Table 4 The IC_{50} values of **3a–3d** against the selected cells for 48 h (μM)

Compound	BGC-823	BEL-7402	MCF-7	A549	HL-7702
3a	12.32 ± 0.37	33.97 ± 2.37	34.32 ± 0.95	16.71 ± 1.50	>100
3b	26.79 ± 0.75	17.60 ± 1.11	7.01 ± 0.26	14.80 ± 0.50	31.56 ± 0.71
3c	9.12 ± 0.19	10.22 ± 0.12	7.05 ± 0.05	7.32 ± 0.05	>100
3d	16.85 ± 0.66	11.14 ± 1.02	10.39 ± 0.52	12.61 ± 0.09	>100
5-FU	15.18 ± 0.05	15.81 ± 0.01	11.32 ± 0.78	11.77 ± 0.89	20.83 ± 0.05
Erlotinib	>20	>20	>20	17.32 ± 3.11	—
Sorafenib	6.08 ± 0.06	5.06 ± 0.02	7.06 ± 0.50	12.25 ± 0.42	—

© 2025 The Author(s). Published by the Royal Society of Chemistry

Open Access Article. Published on 02 January 2025. Downloaded on 3/17/2026 5:53:47 PM. This article is licensed under a Creative Commons Attribution-NonCommercial 3.0 Unported Licence.

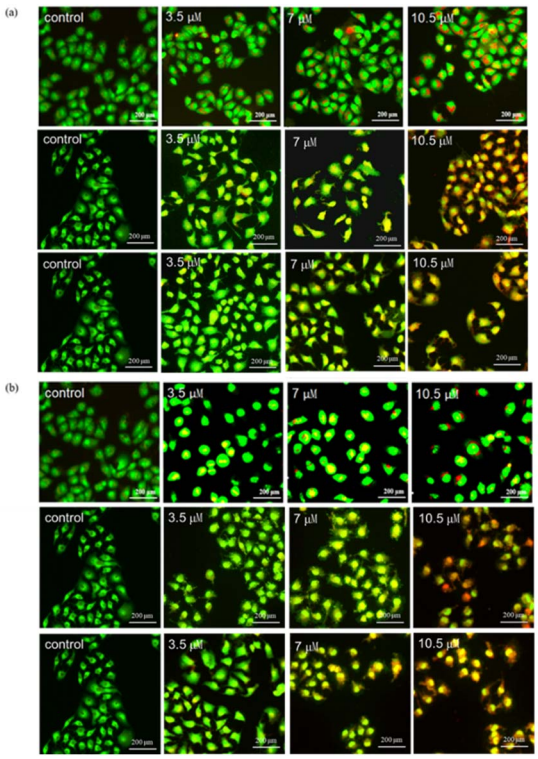

Fig. 5 Changes in morphology of AO/EB double stained MCF-7 cells treated with (a) **3b** and (b) **3c** (3.5 μM, 7 μM and 10.5 μM) for 24 h. (Three independent experiments were performed on each compound.)

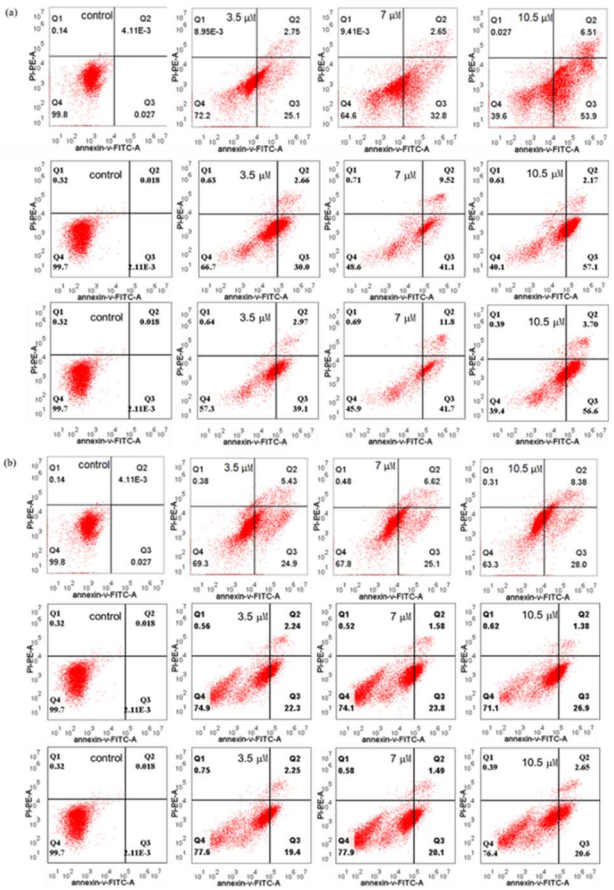

Fig. 6 Apoptosis of MCF-7 cells treated with (a) **3b** and (b) **3c** (0 μM, 3.5 μM, 7 μM and 10.5 μM) for 48 h. (Three independent experiments were performed on each compound.)

25.5%, 26.2%, 29.3%, respectively. The results revealed that both **3b** and **3c** could effectively trigger concentration dependent apoptosis of MCF-7 cells, which was consistent with that of AO/EB double staining.

3.5.3. Generation of ROS in MCF-7 cells. Reactive oxygen species (ROS) play the essential role in regulating immune responses, including anticancer, antibacterial and antiviral responses.[48,49] So, it is vital to quantitatively detect them in biological samples. ROS are mainly produced by mitochondria, which are key substances that lead to the apoptosis process.[50,51] DCFH-DA is often used to investigate the intracellular ROS generation.[45] Fig. 7a and b showed the number of MCF-7 cells and the intracellular ROS intensity in MCF-7 cells increased with the concentration increase of **3b** and **3c** (3.5 μM and 7 μM). Fig. 7c revealed the quantitative changes of intracellular fluorescence intensity with the concentration increase of **3b**. Herein, the fluorescence intensity of the control group and Rosup group were zero and 2.24, respectively. While, in the presence of **3b** (3.5 μM and 7 μM), the fluorescence intensities of DCF increased dramatically to 72.7 and 85.6, which showed a concentration dependence. The results indicated that **3b** can enhance the level of the intracellular ROS and facilitate cells apoptosis, which has also been previously reported.[52,53]

3.6. Discussion of molecular docking

Molecular docking is a commonly used computational method aimed at predicting the binding mode and binding affinity of small molecules with DNA or proteins.[54] Herein, molecular docking was used to investigate the binding mode of **3b** or **3c** with DNA (PDB ID: 2MG8) by AutoDock Tools-1.5.6 and PyMOL Molecular Graphics System. In the docking simulations, the structures of all the compounds were kept flexible. Fig. 8a and b depicted the docked conformations, and the visual diagram showed that **3b** and **3c** binding with DNA adopted a nearly vertical insert mode. The binding energy (ΔG_b^{θ}) of **3b** and **3c** with DNA (PDB ID: 2MG8) was listed in Table 5. The ΔG_b^{θ} of **3b** and **3c** were −7.9 kcal mol^{-1} and −7.2 kcal mol^{-1}, which indicated that the binding of **3b** and **3c** with DNA is spontaneous process. In general, the lower the binding energy, the stronger is the binding affinity.[55] Thus, the binding affinity of **3b** with DNA was slightly larger than that of **3c**. The binding constants (K_b) of **3b** and **3c** calculated according to eqn (1) (ref. 56) are listed in a Table 5. The K_b were 6.53 × 10^5 M^{-1} and 2.00 × 10^5 M^{-1}, respectively, which fall in the range of the insertion mode (1 × 10^5–1 × 10^{11} M^{-1}).[57,58] According to molecular docking, the interaction mode of **3b** and **3c** with DNA was insertion. In addition, Fig. 8 and S33† depicted the hydrogen bonding interaction between **3b** or **3c** with DNA *via* the N atoms of small molecules (**3b** or **3c**) and the H atoms of DNA base. As shown in Fig. 8, the docking active sites of **3b** and **3c** with DNA mainly lie

Open Access Article. Published on 02 January 2025. Downloaded on 3/17/2026 5:53:47 PM. This article is licensed under a Creative Commons Attribution-NonCommercial 3.0 Unported Licence.

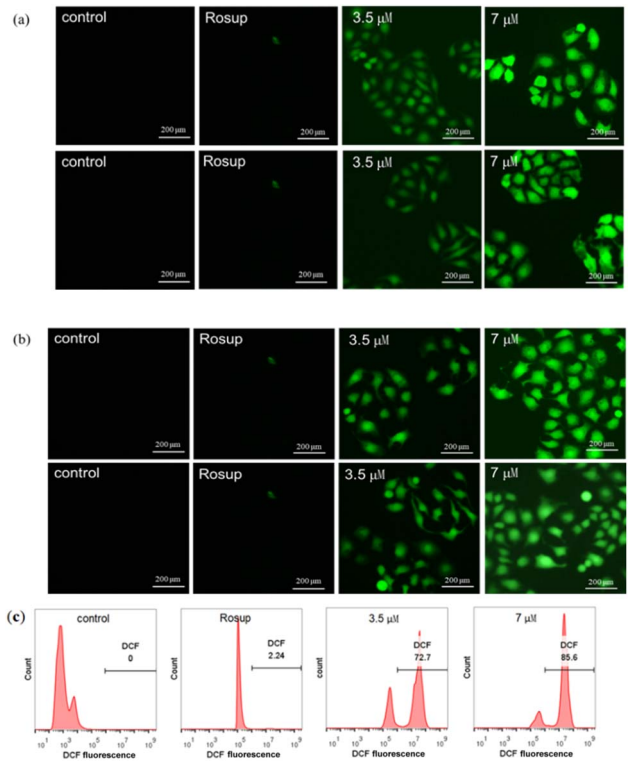

Fig. 7 The inverted fluorescence microscope detection for the ROS fluorescence changes of MCF-7 cells treated with (a) **3b** and (b) **3c** (0 μM, 3.5 μM and 7 μM) for 24 h (independent experiments were performed on each compound). The flow cytometry detection for the ROS fluorescence changes of MCF-7 cells treated with (c) **3b**.

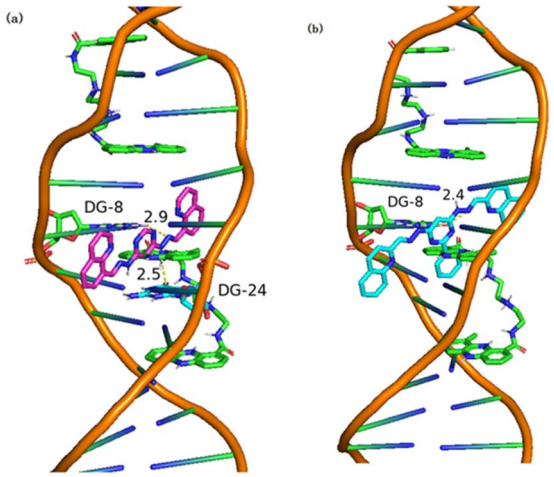

Fig. 8 Visualizations of (a) **3b** and (b) **3c** docking with DNA (PDB ID: 2MG8).

on the T and C base pairs of DNA base pairs. The N atoms in **3b** interacts with DG-8 and DG-24 bases to form hydrogen bonds (Fig. 8a), while **3c** forms hydrogen bonds with DNA only with DG-8 bases (Fig. 8b).

$$\Delta G_b{}^{\theta} = -RT \ln K_b \quad (2)$$

Table 5 The $\Delta G_b{}^{\theta}$ and K_b of **3b** and **3c** interacting with DNA (PDB ID: 2MG8)

Compound	$\Delta G_b{}^{\theta}$ (kcal mol^{-1})	K_b (M^{-1})
3b	−7.9	6.53×10^5
3c	−7.2	2.00×10^5
5-FU	−4.4	1.74×10^3

3.7. Architecture of the CDK2 active site

Similarly, molecular docking is performed to predict the active conformation of a compound with target protein active sites and evaluate their binding affinity, molecular docking is typically performed. CDK2 was also regarded as a potentially therapeutic target for compounds containing pyrimidine units.[59] Therefore, the interactions of **3a–3d** with CDK2 were explored by molecular docking. The $\Delta G_b{}^{\theta}$ of **3a–3d** interacting with CDK2 (PDB ID: 4BGH) were summarized in Table S1.† **3a–3d** all showed interaction with CDK2 to some extent. Among them, **3b** and **3c** showed a slightly stronger interaction with CDK2 than that of **3a** and **3d**, which was in good agreement with the results of cytotoxicity. The 3D and 2D diagrams of **3b** and **3c** docking pose in the active site of CDK2 were shown in Fig. 9. The results revealed different molecular interactions, *e.g.*, hydrogen bonding, π–π interactions and electrostatic attraction between hydrazones and CDK2. As shown in Fig. 9, **3b** exhibits pronounced hydrogen bonding through the nitrogen atoms of the hydrazone linkage with amino acid residues Lys-88. While for **3c**, the hydrogen bonding is formed by hydrogen atoms of hydrazone linkage with amino acid residue Arg-199. In addition, for **3b**, the π–π interactions of the quinoline rings or a pyrimidine ring with amino acid residue Ala-201 and Asp-92 are observed. However, for **3c**, it can be clearly seen that the π–π interactions exists only in the pyrimidine rings with amino acid residue Asp-92. It is probably due to the introduction of benzene ring, which increased the steric hindrance. The results of docking suggested that CDK2 may be one of the targets for **3b** and **3c**. To further investigate whether **3b** and **3c** interact with other CDKs, molecular docking was used to align **3b** and **3c** with CDK1 (6GU7), CDK4 (2W9Z) and CDK8 (5I5Z). The values of $\Delta G_b{}^{\theta}$ were summarized in Table S2–S5.† Overall, the interaction between **3c** and the three CDKs was stronger than that of **3b**, consistent with the previous molecular docking results. CDK1 and CDK8 were selected to dock with **3b** and **3c** for visualization, and the binding modes were obtained, as shown in Fig. 9e–l. It was observable that **3b** forms hydrogen bonds with the amino acid residue Gln-132 of protein CDK1, **3c** forms hydrogen bonds with the amino acid residue Asn-133 of protein CDK1, and with the amino acid residue Val-27 of protein CDK8. The distances of the formed hydrogen bonds were significantly shorter than the conventional hydrogen bond distance of 3.5 Å, and the strong binding plays a crucial role in anchoring small molecules within the protein pocket. Besides hydrogen bonding, there were also hydrophobic forces existing with some amino acid residues, such as Lys-133, Phe-80, Leu-83 and Leu-135 of CDK1, and Val-35, Ala-50, Ala-155 and Arg-356 of

© 2025 The Author(s). Published by the Royal Society of Chemistry

Open Access Article. Published on 02 January 2025. Downloaded on 3/17/2026 5:53:47 PM. This article is licensed under a Creative Commons Attribution-NonCommercial 3.0 Unported Licence.

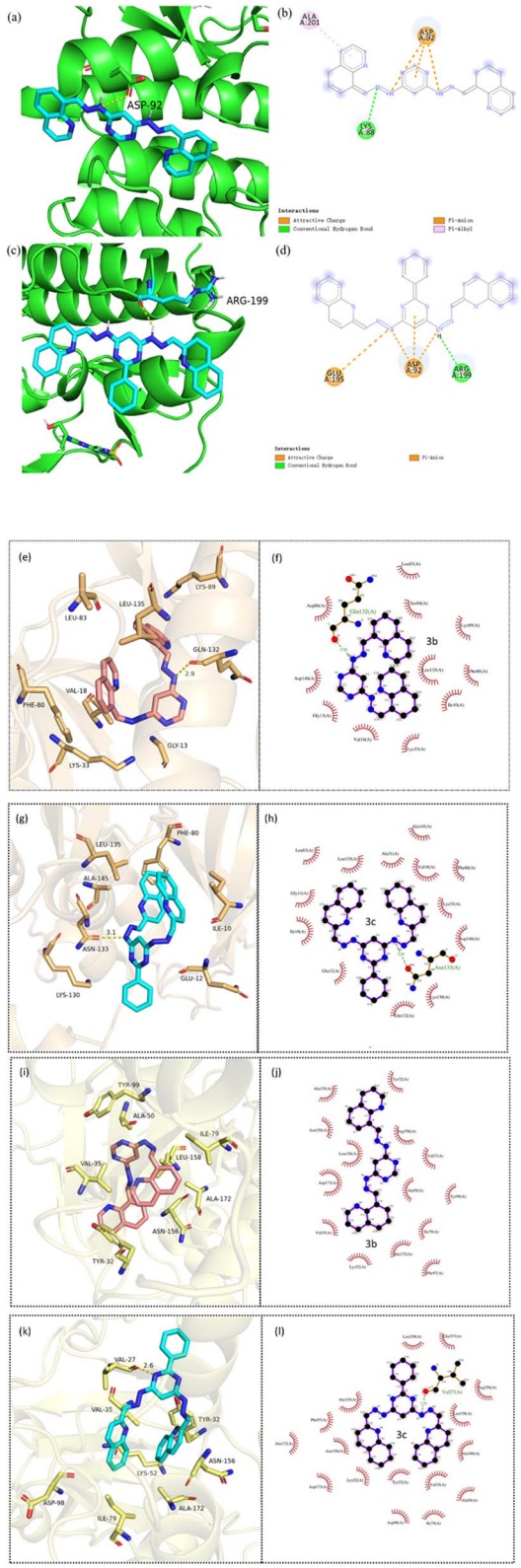

Fig. 9 3D diagram of (a, e and i) **3b** and (c, g and k) **3c** docking pose in the active site of CDK2, CDK1 and CDK8 (PDB: 4BGH; 6GU7; 5I5Z); 2D diagram of (b, f and i) **3b** and (d, h and l) **3c** docking pose in the active site of CDK2, CDK1 and CDK8.

CDK8. To sum up, these interactions enhanced the stability of **3b** and **3c** in the binding pockets of CDK1 and CDK8 proteins and formed stable complexes. Consequently, **3b** and **3c** may possess potential activity against CDK1 and CDK8.

4. Conclusion

In this work, a series of dihydrazone derivatives (**3a–3d**) were synthesized and their nitrosamine impurities were evaluated as well as antiproliferative activity and toxicity were evaluated. The assessment results of nitrosamines indicated that the risk of forming nitrosamine impurities in the final drug was relatively low. Moreover, highly carcinogenic NDMA and NDEA were not detected. Toxicological studies examined the safety profile of **3a–3d**. MTT results showed that they all displayed broad-spectrum antiproliferative activity against selected cancer cell lines (BGC-823, BEL-7402, MCF-7 and A549). It is worth mentioning that **3b** and **3c** displayed more potent antiproliferative activity against MCF-7 cells than 5-FU and Erlotinib with IC_{50} values of 7.016 μM and 7.05 μM, respectively. Results of the apoptosis study showed that compounds **3b** and **3c** increased the number of late apoptotic and early apoptotic cells. AO/EB staining, elevated intracellular ROS levels demonstrated the induction of apoptosis by **3b** and **3c**. **3c** could induce MCF-7 cell apoptosis in a concentration-dependent manner and bind to DNA *via* partial insertion. Additionally, the molecular docking simulations performed for the selected active compound – **3b**, **3c** revealed that they could occupy the active site of CDK1, CDK4 and CDK8 through hydrophobic and H-bonding interactions, which were suggested to be essential for inhibitory activity. This work revealed that quinoline-based dihydrazone derivatives could be used as promising anticancer agents.

Data availability

The authors confirm that the data supporting the findings of this study are available within the manuscript and its ESI.†

Author contributions

Jia-Xing Lu: conceptualization, validation, formal analysis, writing-original draft, writing-review & editing. Hai-Rong Lan: conceptualization, software, investigation. Dai Zeng: software, data curation, investigation. Jun-Ying Song: visualization, investigation. Ya-Ting Hao: investigation, methodology. Ai-Ping Xing, Ao Shen and juan Yuan: conceptualization, methodology, writing-review & editing. All authors provided their final consent for the publication and accepted responsibility for the work conducted in this study.

Conflicts of interest

All authors declare that they have no relevant conflict of interest.

© 2025 The Author(s). Published by the Royal Society of Chemistry

Open Access Article. Published on 02 January 2025. Downloaded on 3/17/2026 5:53:47 PM. This article is licensed under a Creative Commons Attribution-NonCommercial 3.0 Unported Licence.

Acknowledgements

This research was supported by the National Natural Science Foundation of China (Project No. 22101076), the Natural Science Foundation of Henan Province, China (Project No. 202300410261). The authors would like to thank the Shiyanjia lab (**https://www.shiyanjia.com/**) for the support of ^{1}H NMR, ^{13}C NMR, XRD, TG and ESI-HRMS analysis.

Notes and references

1 T. I. De Santana, M. De Oliverira Barbosa, P. A. T. De Moraes Gomes, A. C. N. Da Cruz, T. G. Da Silva and A. C. L. Leite, *Eur. J. Med. Chem.*, 2018, **144**, 874–886.
2 L. Wayteck, K. Breckpot, J. Demeester, S. C. De Smedt and K. Raemdonck, *Cancer Lett.*, 2014, **352**, 113–125.
3 K. Lal and P. Yadav, *Med. Chem.*, 2018, **18**, 21–37.
4 R. Kaur and K. Kumar, *Eur. J. Med. Chem.*, 2021, **215**, 113220.
5 S. Kwon, Y. Lee, Y. Jung, J. H. Kim, B. Baek, B. Lim, J. Lee, I. Kim and J. Lee, *Eur. J. Med. Chem.*, 2018, **148**, 116–127.
6 A. A. Abu-Hashem, O. Hakami and N. Amri, *Heliyon*, 2024, **10**, e26735.
7 Y. Cai, H. Liu and H. F. Chen, *Chem. Biol. Drug Des.*, 2018, **91**, 805–816.
8 A. Baba, N. Kawamura, H. Makino, Y. Ohta, S. Taketomi and T. Sohda, *J. Med. Chem.*, 1996, **39**, 5176–5182.
9 R. Chopra, K. Chibale and K. Singh, *Eur. J. Med. Chem.*, 2018, **148**, 39–53.
10 A. A. Abu-Hashem and N. Amri, *Pharmaceuticals*, 2022, **15**, 1232.
11 H. Cheng, W. Q. Wang, L. Huang, P. Cui and Q. Y. Wu, *Chin. J. Org. Chem.*, 2016, **36**, 1065–1072.
12 V. Srivastava, A. S. Negi, J. K. Kumar, M. M. Gupta and S. P. S. Khanuja, *Bioorg. Med. Chem.*, 2005, **13**, 5892–5908.
13 K. G. Byler, C. Wang and W. N. Setzer, *J. Mol. Model.*, 2009, **15**, 1417–1426.
14 C. H. Xu, W. J. Zhou, G. J. Dong, H. Qiao, J. D. Peng, P. F. Jia, Y. H. Li, H. M. Liu, K. Sun and W. Zhao, *Bioorg. Chem.*, 2020, **105**, 104424.
15 P. Kodisundaram, S. Amirthaganesan and T. Balasankar, *J. Agric. Food Chem.*, 2013, **61**, 11952–11956.
16 J. Amato, R. Morigi, B. Pagano, A. Pagano, A. Ohnmacht, A. De Magis, Y. P. Tiang, G. Capranico, A. Locatelli, A. Graziadio, A. Leoni, M. Rambaldi, E. Novellino, S. Neidle and A. Randazzo, *J. Med. Chem.*, 2016, **59**, 5706–5720.
17 O. I. El-Sabbagh and H. M. Rady, *Eur. J. Med. Chem.*, 2009, **44**, 3680–3686.
18 C. M. Moldovan, O. Oniga, A. B. Tiperciuc, P. Verite, A. Pîrnau, O. Crisan, M. Bojita and R. Pop, *Eur. J. Med. Chem.*, 2011, **46**, 526–534.
19 M. Qin, X. Zhai, H. B. Xie, J. J. Ma, K. Lu, Y. Wang, L. H. Wang, Y. C. Gu and P. Gong, *Eur. J. Med. Chem.*, 2014, **23**, 47–58.
20 K. D. Katariya, S. R. Shah and D. Reddy, *Bioorg. Chem.*, 2020, **94**, 103406.
21 L. Shi, J. J. Xu, J. J. Bi, Z. G. Zhang, T. X. Liu, X. L. Yang and G. S. Zhang, *Chin. J. Org. Chem.*, 2018, **38**, 3016–3025.
22 M. Korcz, F. Sączewski, P. J. Bednarski and A. Kornicka, *Molecules*, 2018, **23**, 1497.
23 J. A. Makawana, C. B. Sangani, L. Lin and H. L. Zhu, *Bioorg. Med. Chem. Lett.*, 2014, **24**, 734–1736.
24 Y. L. Chen, Y. L. Zhao, C. M. Lu, C. C. Tzeng and J. P. Wang, *Bioorg. Med. Chem.*, 2006, **14**, 4373–4378.
25 R. C. Montenegro, L. V. Lotufo, M. O. De Moraes, C. Pessoa, F. A. R. Rodrigues, M. De Lima Ferreira Bispo, C. De Alcantara, C. R. Kaiser and M. V. De Souza, *Med. Chem. Res.*, 2012, **21**, 3615–3619.
26 D. Senthil Raja, N. S. Bhuvanesh and K. Natarajan, *Eur. J. Med. Chem.*, 2012, **47**, 73–85.
27 J. Yuan, J. Y. Song, H. H. Yang, H. R. Lan, A. P. Xing, K. H. Li, D. Zeng, Z. Q. Zhang and S. Y. Feng, *J. Mol. Struct.*, 2023, **1276**, 134724.
28 N. Pawar, A. Bhardwaj, A. Vora and S. Sharma, *J. Chromatogr. A*, 2024, **1**, 1732.
29 O. Afzal, S. Kumar, R. Ali, R. Kumar, M. Jaggi and S. Bawa, *Eur. J. Med. Chem.*, 2015, **97**, 871–910.
30 P. Yadav and K. Shah, *Bioorg. Chem.*, 2021, **109**, 104639.
31 H. Y. Sun, Z. Nikolovska-Coleska, C. Y. Yang, D. Qian, J. Lu, S. Qiu, L. Bai, Y. Peng, Q. Cai and S. Wang, *Acc. Chem. Res.*, 2008, **41**, 1264–1277.
32 D. Moreau, C. Jacquot, P. Tsita, I. Chinou, C. Tomasoni, M. Juge, E. Antoniadou-Vyza, L. Martignat, A. Pineau and C. Roussakis, *Int. J. Cancer*, 2008, **123**, 2676–2683.
33 J. Králová, T. Bríza, I. Moserová, B. Dolenský, P. Vasek, P. Kejík, Z. Poucková, R. Kaplánek, P. Martásek, M. Dvorák and V. Král, *J. Med. Chem.*, 2008, **51**, 5964–5973.
34 S. Okten, O. Cakmak, S. Tekin and T. K. Koprulu, *Lett. Drug Des. Discovery*, 2017, **14**, 1415–1424.
35 M. Peyressatre, C. Prevel, M. Pellerano and M. C. Morris, *Cancers*, 2015, **7**, 179–237.
36 S. R. Whittaker, A. Mallinger, P. Workman and P. A. Clarke, *Pharmacol. Ther.*, 2017, **173**, 83–85.
37 A. B. Heptinstall, I. Adiyasa, C. Cano and I. R. Hardcastle, *Future Med. Chem.*, 2018, **10**, 1369–1388.
38 C. Thangavel, E. Boopathi, Y. Liu, C. McNair, A. Haber, M. Perepelyuk, A. Bhardwaj, S. Addya, A. Ertel, S. Shoyele, R. Birbe, J. M. Salvino, A. P. Dicker, K. E. Knudsen and R. B. Den, *Clin. Cancer Res.*, 2018, **24**, 1402–1414.
39 L. M. Spring, S. A. Wander, M. Zangardi and A. Bardia, *Curr. Oncol. Rep.*, 2019, **21**, 25.
40 M. M. Al-Sanea, A. J. Obaidullah, M. E. Shaker, G. Chilingaryan, M. M. Alanazi, N. A. Alsaif, H. M. Alkahtani, S. A. Alsubaie and M. A. Abdelgawad, *Molecules*, 2021, **26**, 412.
41 T. Mosmann, *J. Immunol. Methods*, 1983, **65**, 55–63.
42 T. Efferth, *Planta Med.*, 2010, **76**, 1035–1036.
43 D. P. Bezerra, F. O. D. Castro, A. P. N. N. Alves, C. Pessoa, M. O. D. Moraes, E. R. Silveira, M. A. S. Lima, F. J. M. Elmiro, N. M. N. D. Alencar, R. O. Mesquita, M. W. Lima and L. V. Costa-Lotufo, *J. Appl. Toxicol.*, 2007, **28**, 156–163.

© 2025 The Author(s). Published by the Royal Society of Chemistry

Open Access Article. Published on 02 January 2025. Downloaded on 3/17/2026 5:53:47 PM.
This article is licensed under a Creative Commons Attribution-NonCommercial 3.0 Unported Licence.

44 E. Ramachandran, V. Gandin, R. Bertani, P. Sgarbossa, K. Natarajan, N. S. P. Bhuvanesh, A. Venzo, A. Zoleo, A. Glisenti, A. Dolmella, A. Albinati and C. Marzano, *J. Inorg. Biochem.*, 2018, **182**, 18–28.
45 G. B. Jiang, Y. Y. Xie, G. J. Lin, H. L. Huang, Z. H. Liang and Y. J. Liu, *J. Photochem. Photobiol., B*, 2013, **129**, 48–56.
46 K. J. Du, J. Q. Wang, J. F. Kou, G. Y. Li, L. L. Wang, H. Chao and L. N. Ji, *Eur. J. Med. Chem.*, 2011, **46**, 1056–1065.
47 X. Q. Zhou, Y. Li, D. Y. Zhang, Y. Nie, Z. J. Li, W. Gu, X. Liu, J. L. Tian and S. P. Yan, *Eur. J. Med. Chem.*, 2016, **114**, 244–256.
48 Y. Han, Z. Tian, S. Zhang, X. Liu, J. Li, Y. Li, Y. Liu, M. Gao and Z. Liu, *J. Inorg. Biochem.*, 2018, **189**, 163–171.
49 M. E. Juan, U. Wenzel, H. Daniel and J. M. Planas, *J. Agric. Food Chem.*, 2008, **56**, 4813–4818.
50 P. Li, Q. L. Zhao, L. H. Wu, P. Jawaid, Y. F. Jiao, M. Kadowaki and T. Kondo, *Apoptosis*, 2014, **19**, 1043–1053.
51 L. Diebold and N. S. Chandel, *Free Radical Biol. Med.*, 2016, **100**, 86–93.
52 J. Deng, J. Wang, M. Khan, P. Yu, F. Yang and H. Liang, *J. Inorg. Biochem.*, 2018, **185**, 10–16.
53 M. H. Khan, M. Cai, J. Deng, P. Yu, H. Liang and F. Yang, *Molecules*, 2019, **24**, 2544.
54 M. C. Zhu, X. T. Cui, F. C. Zhao, X. Y. Ma, Z. B. Han and E. J. Gao, *RSC Adv.*, 2015, **5**, 47798–47808.
55 M. L. Liu, M. Jiang, K. Zheng, Y. T. Li, Z. Y. Wu and C. W. Yan, *J. Coord. Chem.*, 2014, **67**, 630–648.
56 M. N. Zafar, A. M. Butt, G. E. Chaudhry, F. Perveen, M. F. Nazar, S. Masood, A. F. Dalebrook, E. U. Mughal, S. U. Sumrra, Y. Y. Sung, T. S. T. Muhammad and L. J. Wright, *J. Inorg. Biochem.*, 2021, **224**, 111590.
57 A. Wolfe, H. G. J. Shimer and T. Meehan, *Biochemistry*, 1987, **26**, 6392–6396.
58 X. Q. Zhou, Y. Li, D. Y. Zhang, Y. Nie, Z. J. Li, W. Gu, X. Liu, J. L. Tian and S. P. Yan, *Eur. J. Med. Chem.*, 2016, **3**, 244–256.
59 I. F. Nassar, M. T. Abdel Aal, W. A. El-Sayed, A. E. Shahin M, E. G. E. Elsakka, M. M. Mokhtar, M. Hegazy, M. Hagras, A. A. Mandour and N. S. M. Ismail, *RSC Adv.*, 2022, **12**, 14865–14882.